Title

Influence of conducting plate boundary conditions on the transverse envelope equations describing intense ion beam transport

Journal

Physical Review Special Topics - Accelerators and Beams, 706(6)

Authors

Lund, Steven M.
Bukh, Boris

Publication Date

2003-05-01

Influence of conducting plate boundary conditions on the transverse envelope equations describing intense ion beam transport

Steven M. Lund*
Lawrence Livermore National Laboratory, University of California, Livermore, CA 94550

Boris Bukh
Lawrence Berkeley National Laboratory, University of California, Berkeley, CA 94720
(Dated: July 21, 2003)

In typical diagnostic applications, intense ion beams are intercepted by a conducting plate associated with devices used to measure beam phase-space projections. This results in the transverse space-charge field near the plate being shorted out, rendering simple envelope models with constant space-charge strength inaccurate. Here we develop corrected envelope models based on analytical calculations to account for this effect on the space-charge term of the envelope equations, thereby removing a systematic source of error in the equations and enabling more accurate comparisons with experiment. For common intense beam parameters, we find that the correction occurs primarily in the envelope angles and that the effect can be large enough to degrade precision beam matching. Results are verified with 3D self-consistent PIC simulations based on intense beam experiments associated with driver developments for Heavy-Ion Fusion.

PACS numbers: 29.27.Bd,41.75.-i,52.59.Sa,52.27.Jt

I. INTRODUCTION

Low-order models of intense ion beams often employ the rms envelope equations to describe the self-consistent evolution of the statistical beam edge in response to applied focusing, space-charge, and thermal defocusing forces[1–4]. Such envelope models are typically solved with constant beam emittances (phase-space area) and perveance (space-charge strength) to extrapolate experimental measurements and understand the evolution of the beam envelope away from diagnostic stations. A typical slit-scanner intercepting beam diagnostic used to measure beam phase-space projections is sketched in Fig. 1. In this diagnostic an elliptical cross-section beam emerging from a transport channel free-drifts into a conducting plate with a thin slit that passes a thin ribbon of particles (sized for adequate signal while maintaining good resolution) that is then intercepted by a second nearby slit-plate. The second thin-slit is parallel to the first slit and is combined with a Faraday cup to collect the transmitted component of the beam distribution. By differentially moving the plates in directions perpendicular to the slit axes and recording signals collected, phase-space projections of the beam distribution perpendicular to the slit axis can be unfolded at the axial location of the first plate[5, 6]. Sequences of such diagnostics with orthogonal slits are often employed to measure the evolution of beam phase-space projections from which beam envelope parameters are calculated. Alternatively, optical beam imagers have been employed to measure more complete phase-space data of the beam distribution and envelope projections are made[7]. Both classes of intercepting beam diagnostics are characterized in an approximate fashion by a conducting plate that intercepts the beam at the axial plane of the measurement. The proximity of the conducting plate to the beam upstream will alter electrostatic space-charge forces of an intense beam, modifying the particle dynamics and envelope evolution near the plate. Developing a simple model to compensate for systematic changes in the envelope induced by such plates is needed for more precise estimates of the beam envelope without the need for large simulations. Elimination of systematic errors in envelope modeling can improve the precision of envelope matching which is important in limiting the generation of beam halo and related particle losses.

This paper is organized as follows. In Sec. II an electrostatic beam envelope model is derived with form-factor corrections to the usual envelope equations that account for the presence of conducting surfaces influencing beam self-fields and other space-charge effects. A simple plane in free-space model of end-plate conductors is adopted to represent intercepting diagnostic plates and allow an image-charge solution for the beam self-fields in a form that is convenient for analytical modeling. Particle-in-cell (PIC) simulations of a more realistic version of this geometry based on practical experiments are described in Sec. III. These simulations are used to check assumptions made in later sections to simplify envelope models. The space-charge model is solved for a uniform density, axisymmetric

*smlund@lbl.gov

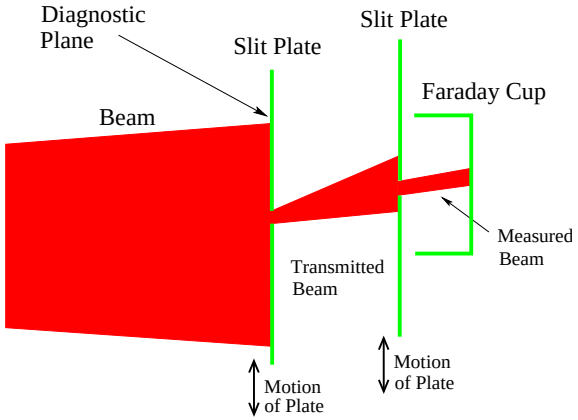

FIG. 1: Cross-section of slit-plate diagnostics for measurement of beam phase-space.

($\partial/\partial\theta = 0$) beam in Sec. IV. Analytical field solutions are employed to calculate form-factors and derive a heuristic corrected envelope equation for an axisymmetric beam in the presence of the conducting plate. Model predictions are verified with PIC simulations. Insights gained in Sec. IV are then applied to the more difficult case of a uniform density elliptical beam in Sec. V, where a more approximate corrected envelope equation is derived and again verified with simulations.

II. ENVELOPE MODEL

Consider a long-pulse, unbunched beam with particles of charge q and mass m moving with axial velocity $\beta_b c$ and relativistic factor $\gamma_b = 1/\sqrt{1-\beta_b^2}$. We take the transverse orbits $x(s)$ and $y(s)$ of a beam particle to satisfy the paraxial (axial energy variation of particles neglected) equations of motion[1]

$$\begin{aligned} x'' + \kappa_x x + \frac{q}{m\gamma_b^3\beta_b^2 c^2}\frac{\partial\phi}{\partial x} = 0, \\ y'' + \kappa_y y + \frac{q}{m\gamma_b^3\beta_b^2 c^2}\frac{\partial\phi}{\partial y} = 0. \end{aligned} \tag{1}$$

Here, s is the axial coordinate of a beam slice, primes denote derivatives with respect to s, $\kappa_x(s)$ and $\kappa_y(s)$ are the linear applied focusing functions of the lattice, and the electrostatic potential ϕ is related to the number density of beam particles n by the 3D Poisson equation

$$\nabla^2\phi = -\frac{q}{\epsilon_0}n \tag{2}$$

subject to $\phi = \text{const}$ on conducting boundaries. Here, ϵ_0 is the permitivity of free-space, and MKS units are employed except where otherwise noted. Specific forms of the focusing functions κ_x and κ_y are given for various classes of transport lattices in Ref. [2].

Denote a transverse average over an axial slice of beam particles by $\langle\cdots\rangle_\perp$. RMS measures of the transverse edge radii of the beam envelope are

$$\begin{aligned} r_x(s) = 2\sqrt{\langle x^2\rangle_\perp}, \\ r_y(s) = 2\sqrt{\langle y^2\rangle_\perp}. \end{aligned} \tag{3}$$

The statistical envelope radii r_x and r_y correspond to the transverse edge-radii of a uniform density beam slice of elliptical transverse cross-section with principal axes aligned with the x- and y-coordinate axes. Differentiating the equations for r_x and r_y and employing Eq. (1) yields the envelope equations

$$\begin{aligned} r_x'' + \kappa_x r_x - \frac{2Q}{r_x + r_y}F_x - \frac{\epsilon_x^2}{r_x^3} = 0, \\ r_y'' + \kappa_y r_y - \frac{2Q}{r_x + r_y}F_y - \frac{\epsilon_y^2}{r_y^3} = 0. \end{aligned} \tag{4}$$

Here,

$$Q = \frac{q\lambda}{2\pi\epsilon_0 mc^2\gamma_b^3\beta_b^2} = \text{const} \tag{5}$$

is the dimensionless perveance ($\lambda = \text{const}$ is the line-charge density of the beam slice),

$$\begin{aligned} F_x &= -\frac{4\pi\epsilon_0}{\lambda}\left(\frac{r_x + r_y}{r_x}\right)\langle x\frac{\partial\phi}{\partial x}\rangle_\perp, \\ F_y &= -\frac{4\pi\epsilon_0}{\lambda}\left(\frac{r_x + r_y}{r_y}\right)\langle y\frac{\partial\phi}{\partial y}\rangle_\perp, \end{aligned} \tag{6}$$

are form-factors, and

$$\begin{aligned} \varepsilon_x &= 4\left[\langle x^2\rangle_\perp\langle x'^2\rangle_\perp - \langle xx'\rangle_\perp^2\right]^{1/2}, \\ \varepsilon_y &= 4\left[\langle y^2\rangle_\perp\langle y'^2\rangle_\perp - \langle yy'\rangle_\perp^2\right]^{1/2} \end{aligned} \tag{7}$$

are the rms edge-emittances.

For the special case of a 2D ($\partial/\partial z = 0$) transverse beam in free-space with constant charge density on nested elliptical surfaces with principal semi-axes αr_x and αr_y aligned with the x- and y-coordinate axes, Sacherer[3] analyzed beam self-fields and showed that $F_x = F_y = 1$. The Vlasov model self-consistent KV distribution satisfies this condition for the special case of a uniform density elliptical beam with constant emittances $\epsilon_x = \text{const}$ and $\epsilon_y = \text{const}$[1, 4]. The envelope equations (4) are also often applied with $F_x = F_y = 1$ in an rms equivalent beam sense[1, 3]. By calculating the form factors F_x and F_y as a function of r_x and r_y (and possibly other s-varying quantities) in specific geometries for given beam charge distribution, the envelope equations (4) can be compensated for effects such as evolving space-charge nonuniformities and conductor boundary conditions (often called image charges). In this paper we address a specific form of image-charge compensations associated with conducting plates intercepting the beam. Formally, Eqs. (4) are consistent with constant emittances only when the electric self-field components

$$\begin{aligned} E_x &= -\frac{\partial\phi}{\partial x}, \\ E_y &= -\frac{\partial\phi}{\partial y} \end{aligned} \tag{8}$$

used in calculating F_x and F_y are linear functions of x and y, respectively, within the beam. However, Eqs. (4) are sometimes solved with F_x and F_y calculated with nonlinear linear terms in E_x and E_y *and* constant emittances. The efficacy of such non-consistent orderings must be established for logical consistency if such nonlinear perveance terms are employed to claim more accurate estimates of envelope evolutions with Eq. (4) because emittance evolutions consistent with self-field nonlinearities can also influence the envelope evolution. Unfortunately, such consistency checks have rarely been carried out in the literature when nonlinear self-field terms are included in moment corrections. In Sec. IV we address this issue by making comparisons of corrected moment envelope model results derived with both linear and nonlinear self-field models to self-consistent PIC simulations.

For purposes of deriving analytical models, we idealize the geometry as a beam impinging on a perfectly conducting plane at $z = 0$ in free-space from $z < 0$ as sketched in Fig. 2. In this situation the method of images can be used to solve for ϕ in the beam region with $z < 0$ as

$$\phi(\mathbf{x}) = \frac{q}{4\pi\epsilon_0}\int_{\text{beam}} d^3\tilde{x}\ \left[\frac{n(\tilde{\mathbf{x}})}{|\mathbf{x} - \tilde{\mathbf{x}}|} - \frac{n(\tilde{\mathbf{x}}_I)}{|\mathbf{x} - \tilde{\mathbf{x}}_I|}\right]. \tag{9}$$

Here, $\mathbf{x} = x\hat{\mathbf{x}} + y\hat{\mathbf{y}} + z\hat{\mathbf{z}}$ and $\mathbf{x}_I = x\hat{\mathbf{x}} + y\hat{\mathbf{y}} - z\hat{\mathbf{z}}$ are the direct and image coordinates of a beam particle, and we have dropped an arbitrary additive constant to ϕ consistent with taking a bias $\phi = 0$ on the plate. For transverse effects the value of the plate bias is not important. However, if longitudinal acceleration effects induced by the plate are also evaluated, the choice of plate bias can become important.

III. PARTICLE-IN-CELL SIMULATIONS

Self-consistent 3D electrostatic PIC simulations are carried out to validate approximations and model assumptions that are made in subsequent sections to derive approximate form-factors and enable direct solution of the envelope

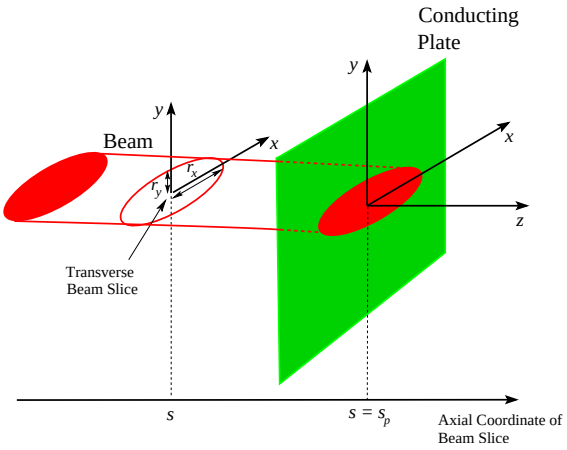

FIG. 2: Geometry of an unbunched beam incident on a conducting plane from the left ($z < 0$).

model. The simulations allow analysis of model deviations resulting from: more realistic geometry, self-field nonlinearities, emittance growth, rapid variations in the beam envelope near the plate, energy deviations due to the beam seeing it's image in the plate, and effects resulting from deviations in the beam transverse cross-sections from simple uniform-density elliptical. In this section we describe the general features of the simulations and numerical parameters. Simulations results are given in Secs. IV and V where comparisons to reduced analytical models are made.

Simulation parameters are based on typical diagnostic measurements in the High Current Experiment (HCX) for Heavy-Ion Fusion (HIF)[5, 6, 8], where an intense K^+ ion beam with particle kinetic energy $\mathcal{E} = 1.0$–1.7 MeV is focused in a FODO quadrupole lattice with period $L_p = 435.2$ mm. At $\mathcal{E} = 1.0$ MeV, injected beam currents are in the range $I \simeq \lambda/\sqrt{2\mathcal{E}/m} = 180$–$250$ mA (corresponding to $Q \sim 7$–$10 \cdot 10^{-4}$) with beam emittances $\varepsilon_x \sim \varepsilon_y \sim 50$–$100$ mm-mrad. Electric quadrupole focusing strengths are tuned for an undepressed single-particle phase advance of $\sigma_0 = 40°$–$90°$ per lattice period. For quadrupole focusing strength with $\sigma_0 = 80°$, a typical matched beam envelope in the HCX periodic transport channel has average envelope radius $(1/L_p)\int_0^{L_p} ds\, r_x(s) \sim 10$ mm and maximum envelope angles are $\mathrm{Max}[|r_x'|] \sim 50$ mrad. Free-drifts ($\kappa_x = \kappa_y = 0$) from the exit of quadrupole focusing elements to conducting plates of slit-scanner diagnostic stations are ~ 70–100 mm.

We employ the 3D WARP code developed for simulation of intense beams in HIF applications[9]. This code has an extensive hierarchy of models allowing both checks of numerical methods and idealizations made. A multi-grid fieldsolver is employed that allows boundaries of detailed conductor structures to be placed at subgrid resolution on the regular parallelpiped grid of the code. To represent HCX-like beams, we carry out steady-state, mid-pulse simulations of a beam injected into a focus-free drift section. In all simulations presented we take $\mathcal{E} = 1.0$ MeV, singly ionized ions with mass $m = 39.1$ amu, and the injected beam current is varied to attain a specified perveance Q. The drift is 70 mm long axially. To reduce the idealization of the geometry taken in Fig. 2, a grounded ($\phi = 0$) cylindrical conducting pipe with radius $r_p = 100$ mm is added. Such pipes or other structures that reduce longitudinal self-field components of the beam are often present in experiments. The beam is injected from the left-side of the grid ($s = 0$) with $\partial\phi/\partial z = 0$ to model a beam entering from a long focusing channel. On the right-side of the grid, the conducting plate at the diagnostic plane ($s = s_p = 70$ mm) is held at $\phi = 0$. The injected beam is "semi-Gaussian" with a uniform distribution of particles coordinates x and y within an elliptical beam envelope with principal axes r_x and r_y along the transverse x- and y-axes. The injected semi-Gaussian beam also has particle angles x' and y' with coherent components $r_x'(x/r_x)$ and $r_y'(y/r_y)$ and incoherent spatially uniform, Gaussian distributed spreads in angles with variances set such that the specified emittances ε_x and ε_y are injected. This injection condition is a reasonable approximation to a relaxed, strongly space-charge dominated beam emerging from a long transport channel where the density is expected to be nearly uniform and the beam-edge sharp[10]. The injected longitudinal velocity spread of the beam is Gaussian distributed with variance set such that the spread in longitudinal particle velocities about the mean velocity set by the specified particle kinetic energy is equal to half the transverse spread in incoherent particle velocities (i.e., the longitudinal temperature in the beam frame is half the transverse temperature).

Numerical parameters of the simulations are set for high resolution to resolve nonlinear space-charge fields and a sharp beam edge. Spatial grids are uniform with typical transverse grid increments $dx = dy \sim 0.2$–0.4 mm and axial grid increment $dz \sim 0.2$–0.8 mm, corresponding to ~ 25–50 grids across the transverse radius of the beam and ~ 80–350 grids along the longitudinal axis of the beam. An axisymmetric r–z fieldsolver is used in place of the full three-dimensional fieldsolver in cases where an axisymmetric beam is injected with $r_x(0) = r_y(0)$ and $r_x'(0) = r_y'(0)$, and 4-fold transverse symmetry is used for elliptical beam injections with $r_x(0) \neq r_y(0)$ and/or $r_x'(0) \neq r_y'(0)$. Exploiting

these symmetries allows more rapid simulations and improved statistics. The same three-dimensional particle mover is used for both axisymmetric and non-axisymmetric injections. Particles are advanced in time with periodic fieldsolves (subcycled relative to particle advances to reduce simulation time, with 5–20 advances per fieldsolve) from injection until exiting the grid at the diagnostic plate where the particle disappears in the simulation. Particles are typically injected for two transit times through the axial grid, allowing transients to propagate off the grid to attain a steady mid-pulse solution. More than 7 million particles fill the grid on the steady-state beam to reduce statistical noise in the calculation of self-fields.

IV. CORRECTED ENVELOPE EQUATIONS FOR AXISYMMETRIC BEAMS

Before proceeding to analyze the more difficult case of an elliptical beam in Sec. V, we first develop modeling techniques for an axisymmetric ($\partial/\partial\theta = 0$) beam with $r_x(s) = r_y(s) = R(s)$[11].

A. Self-Field Solution

We further idealize the beam self-field solution given by Eq. (9) by assuming that the beam is normally incident with uniform density and a constant, round edge-radius ($r_x = r_y = R = \text{const}$). Then the beam density is given by

$$n(r,z) = \frac{\lambda}{\pi q R^2}\Theta(R-r)\Theta(-z), \tag{10}$$

where $\Theta(x)$ is the Heaviside step-function [$\Theta(x) = 0$ for $x < 0$ and $\Theta(x) = 1$ for $x > 0$]. In (r,θ,z) cylindrical coordinates with $x = r\cos\theta$ and $y = r\sin\theta$, $1/|\mathbf{x}-\tilde{\mathbf{x}}|$ can be expanded as[12, p. 131]

$$\frac{1}{|\mathbf{x}-\tilde{\mathbf{x}}|} = \sum_{\nu=-\infty}^{\infty}\int_0^\infty dk\; e^{i\nu(\theta-\tilde{\theta})}J_\nu(kr)J_\nu(k\tilde{r})e^{k(z_>-z_<)},$$

where $z_>$ and $z_<$ denote the greater and lesser of z and $\tilde{z}$, and $J_\nu(x)$ is a νth-order ordinary Bessel function. Using this expansion and Eq. (10) in Eq. (9) gives for $z < 0$

$$\phi(r,z) = \frac{\lambda}{\pi\epsilon_0}\int_0^\infty \frac{dw}{w^2}\left(1-e^{-w|z|/R}\right)J_0\left(w\frac{r}{R}\right)J_1(w), \tag{11}$$

and the corresponding radial and axial electric field components $E_r = -\partial\phi/\partial r$ and $E_z = -\partial\phi/\partial z$ are

$$\begin{aligned} E_r(r,z) =& \frac{\lambda}{\pi\epsilon_0 R}\int_0^\infty \frac{dw}{w}\left(1-e^{-w|z|/R}\right)J_1\left(w\frac{r}{R}\right)J_1(w), \\ E_z(r,z) =& \frac{\lambda}{\pi\epsilon_0 R}\int_0^\infty \frac{dw}{w}\,e^{-w|z|/R}J_0\left(w\frac{r}{R}\right)J_1(w). \end{aligned} \tag{12}$$

These field components are plotted in Fig. 3. Note that the radial field remains nearly linear within the beam ($r < R$) until z is a fraction of a beam radius from the plate. The axial field increases with decreasing $|z|$ because the negative image beam becomes closer as the plate is approached.

Equations (12) are checked by calculating the radial field far from the plate and the longitudinal field on-axis ($r = 0$):

$$\begin{aligned} \lim_{|z|\to\infty} E_r(r,z) &= \frac{\lambda}{\pi\epsilon_0 R}\int_0^\infty \frac{dw}{w}\,J_1\left(w\frac{r}{R}\right)J_1(w) \\ &= \frac{\lambda}{2\pi\epsilon_0 R}\cdot\begin{cases}\frac{r}{R}, & 0\le\frac{r}{R}\le 1,\\ \frac{1}{r/R}, & 1\le\frac{r}{R},\end{cases} \\ E_z(r=0,z) &= \frac{\lambda}{\pi\epsilon_0 R}\int_0^\infty \frac{dw}{w}\,e^{-w|z|/R}J_1(w) \\ &= \frac{\lambda}{\pi\epsilon_0 R^2}\left(\sqrt{R^2+z^2}-|z|\right). \end{aligned} \tag{13}$$

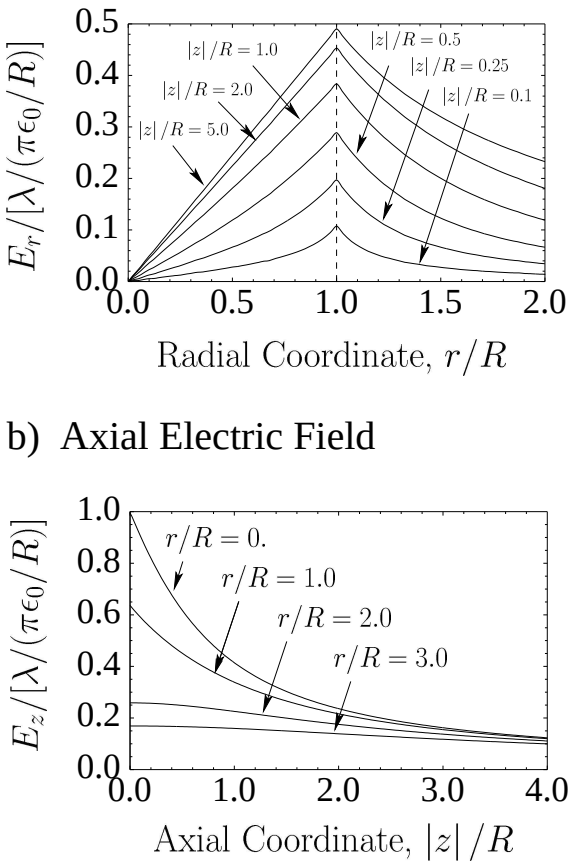

FIG. 3: Radial and axial electric self-field components [Eq. (12)] of a uniform density axisymmetric beam with radius $R = \text{const}$ near a conducting plate. In (a) the scaled radial electric field $E_r/[\lambda/(\pi\epsilon_0 R)]$ is plotted versus r/R in fixed z-planes. In (b) the scaled axial electric field $E_z/[\lambda/(\pi\epsilon_0 R)]$ is plotted versus $|z|/R$ in fixed r-cylinders.

The radial field limit is the usual expression for a uniform density beam of radius R. The expression for the on-axis axial field $E_z(r = 0, z)$ shows that $\phi(r = 0, z)$ logarithmically diverges in $|z|$ with

$$\phi(r = 0, z) = \frac{\lambda}{2\pi\epsilon_0 R^2}\left(|z|\sqrt{R^2 + z^2} - z^2 + R^2 \ln\left[\frac{|z| + \sqrt{R^2 + z^2}}{R}\right]\right).$$

This divergence is related to the 2D nature of the problem and shows that this model is inadequate for direct use in estimates of axial acceleration induced by the plate. Regularization of this divergence to model image induced self-field accelerations can be carried out by adding a grounded, cylindrical pipe to cutoff the self-field interaction range (as would be present in the laboratory) or using a axially-bunched beam model. Even though ϕ is diverging in $|z|$ in this simple model, the formula for E_r can still be applied in Eqs. (1) and (4) when the beam energy is held fixed because the transverse dynamics do not depend on the absolute scale of ϕ. Because little fractional change in particle energy will occur in a high-energy beam when the beam is near the plate and we have neglected such energy changes in our model, regularization of the longitudinal field divergence is not needed to reliably model transverse beam effects in this study.

This simple model can also be used to estimate the scaling in $|z|$ of the transverse potential drop from the radial center ($r = 0$) to edge ($r = R$) of the beam. Equation (11) gives

$$\Delta\phi(z) \equiv \phi(r = 0, z) - \phi(r = R, z) = \frac{\lambda}{\pi\epsilon_0}\int_0^\infty \frac{dw}{w^2}\left(1 - e^{-w|z|/R}\right)[1 - J_0(w)]J_1(w). \tag{14}$$

This formula provides a reliable estimate for $\Delta\phi$ in physical applications even though ϕ diverges in $|z|$ within the model employed because the drop is a relative transverse measure. The potential drop is plotted in Fig. 4. Observe

that $\Delta\phi(z)$ rapidly decreases from the limiting value $\lim_{|z|\to\infty}\Delta\phi = \lambda/(4\pi\epsilon_0)$ to zero near the plate. This shorting out of the transverse ion-beam potential well suggests that any electrons trapped in the ion-distribution will likely be lost near the diagnostic plane. Such effects will become important in diagnostics to measure trapped electron components — a topic not directly addressed in this paper, but of increasing interest in high intensity beam transport[13, 14].

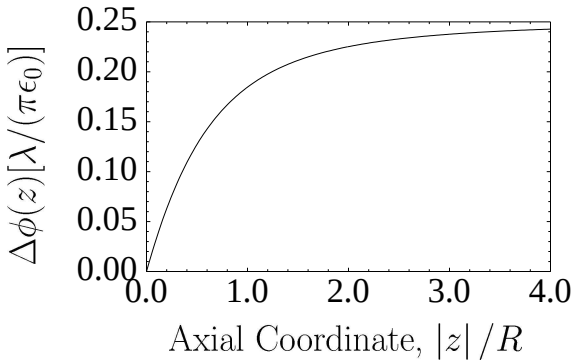

FIG. 4: Radial potential drop of a uniform density axisymmetric beam with radius $R = \text{const}$ near a conducting plate. The potential drop $\Delta\phi(z) = \phi(r = 0, z) - \phi(r = R, z)$ from beam center ($r = 0$) to edge ($r = R$) is normalized by $\lambda/(\pi\epsilon_0)$ and plotted versus $|z|/R$.

B. Corrected Envelope Equation and Results

We apply the self-field solution above to motivate a simple, corrected envelope equation for an axisymmetric beam with a normally incident centroid impinging on a conducting plate from $z < 0$. We take $\kappa_x(s) = \kappa_y(s) \equiv \kappa(s)$, $\varepsilon_x = \varepsilon_y \equiv \varepsilon$, and $r_x(s) = r_y(s) \equiv R(s)$. The form-factors (6) are calculated from Eq. (12) as

$$F_x = F_y = -\frac{4\pi\epsilon_0}{\lambda}\left\langle r\frac{\partial\phi}{\partial r}\right\rangle_\perp = F_a\left(\frac{|z|}{R}\right), \tag{15}$$

where

$$F_a(\zeta) \equiv 8\int_0^\infty \frac{dw}{w^2}\left(1 - e^{-w\zeta}\right) J_1(w)J_2(w). \tag{16}$$

The integral in Eq. (16) can be equivalently calculated as

$$\begin{aligned} F_a(\zeta) &= 2\zeta^2\left[{}_2F_1\left(-\frac{1}{2},\frac{1}{2};2;-\frac{4}{\zeta^2}\right) - 1\right] \\ &= 2\zeta^2\left(\frac{2}{\pi}\int_0^1 dt\,\sqrt{\frac{1-t}{t}}\sqrt{1+\frac{4t}{\zeta^2}} \quad - 1\right). \end{aligned} \tag{17}$$

Here, ${}_2F_1(a, b; c; x)$ is the hypergeometric function with integral representation

$${}_2F_1(a,b;c;x) = \frac{\Gamma(c)}{\Gamma(b)\Gamma(c-b)}\int_0^1 dt\, t^{b-1}(1-t)^{c-b-1}(1-tx)^{-a}$$

and $\Gamma(x) = \int_0^\infty dt\; t^{x-1}e^{-t}$ is the gamma function. We heuristically apply this form-factor to a beam slice with *evolving* radius $r_x(s) = r_y(s) = R(s)$ that is at an axial distance $|z| = |s - s_p|$ from the plate to obtain the corrected axisymmetric beam envelope equation

$$R'' + \kappa\, R - \frac{Q}{R}F_a\left(\frac{|s-s_p|}{R}\right) - \frac{\varepsilon^2}{R^3} = 0. \tag{18}$$

This equation is not self-consistent because the form-factor correction is derived for $R = \text{const}$ but is applied for evolving $R(s)$. However, the error involved in this approximation is expected to be small unless the envelope radius changes rapidly near the plate.

Rather than directly employing Eqs. (16) or (17) to calculate the nonlinear form factor F_a, simpler approximate analytical expressions for F_a can be calculated as follows. In the beam (i.e., $r \le R$ and $z \le 0$), the Poisson equation (2) can be expressed as

$$\left(\frac{1}{r}\frac{\partial}{\partial r}r\frac{\partial}{\partial r} + \frac{\partial^2}{\partial z^2}\right)\phi(r,z) = -\frac{\lambda}{\pi\epsilon_0 R^2}. \tag{19}$$

The solution to this equation can be expanded in a power series in r^2 as

$$\phi(r,z) = \sum_{\nu=0}^{\infty} f_{2\nu}(z) r^{2\nu}, \tag{20}$$

where the $f_{2\nu}(z)$ are z-varying expansion coefficients. Identifying $\phi(r=0,z) = f_0(z)$ and requiring that Eq. (19) is satisfied for all powers of r shows that

$$\begin{aligned} f_0(z) &= \phi(r=0,z), \\ f_{2\nu+2}(z) &= -\frac{\lambda}{4\pi\epsilon_0 R^2}\delta_{0,\nu} - \frac{1}{(2\nu+2)^2}\frac{\partial^2}{\partial z^2} f_{2\nu}(z), \end{aligned} \tag{21}$$

where $\delta_{\mu,\nu}$ is the Kronecker delta function ($\delta_{\mu,\nu} = 1$ when $\mu = \nu$ and $\delta_{\mu,\nu} = 0$ when $\mu \neq \nu$). Using the on-axis field $E_z(r=0,z) = -\partial\phi(r=0,z)/\partial z$ in Eq. (13) and iterating the recursion between terms in Eq. (21), we obtain a series expansion for $E_r(r,z) = -\partial\phi(r,z)/\partial z$ that is valid within the beam:

$$E_r(r,z) = \frac{\lambda}{2\pi\epsilon_0 R^2}\left\{\frac{|z|}{\sqrt{R^2+z^2}}r \; + \sum_{\nu=2,3,\cdots}^{\infty} \frac{(-1)^\nu \nu}{2^{2\nu-2}(\nu!)^2}\frac{\partial^{2\nu-2}}{\partial z^{2\nu-2}}\frac{z}{\sqrt{R^2+z^2}} r^{2\nu-1}\right\}. \tag{22}$$

The first term of this expansion corresponds to the linear self-field component $\propto r$, and the $\nu = 2$ term corresponds to a cubic nonlinear self-field component $\propto r^3$. Using the linear and then the linear plus cubic terms of Eq. (22) in Eq. (15) gives

$$F_a(\zeta) \simeq \begin{cases} \frac{\zeta}{\sqrt{1+\zeta^2}}, & \text{linear term,} \\ \frac{\zeta}{\sqrt{1+\zeta^2}}\left[1 + \frac{1}{4}\frac{1}{1+\zeta^2}\left(1 - \frac{\zeta^2}{1+\zeta^2}\right)\right], & \text{linear plus cubic terms.} \end{cases} \tag{23}$$

The envelope equation (18) with the linear term form-factor in Eq. (23) is consistent with taking emittance $\varepsilon = \text{const}$ because the self-field is taken to be linear in this approximation.

The full nonlinear [Eq. (16) or Eq. (17)] and approximate [Eq. (23)] form-factors are plotted in Fig. 5 versus axial distance from the plate in beam radii $\zeta = |z|/R = |s - s_p|/R$. For large ζ note that $F_a \simeq 1$ and we obtain the usual envelope equations[1], whereas F_a rapidly decreases to zero at $\zeta = 0$ when ζ is decreased to values corresponding to axial distances within the order of a beam radius from the plate. This decrease stems from the radial self-field of the beam being shorted out near the conducting plate, resulting in a decrease in the strength of the perveance term in the envelope equation.

A numerical solution to the corrected envelope equation (18) with $\varepsilon = \text{const}$ is plotted in Fig. 6 together with the uncorrected solution with $F_a = 1$. Parameters chosen represent a typical diagnostic measurement in the HCX experiment described in Sec. III and the corrected solution employs the full nonlinear form-factor given by Eqs. (16) or (17). In Table I, values of the envelope radius R and angle R' at the plate ($s = s_p$) are contrasted for constant emittance numerical solutions to Eq. (18) for a range of beam parameters and initial conditions. Parameters chosen in the first three groups of rows in Table I include the solution shown in Fig. 6 and represent possible ranges of beam parameters for the HCX experiment and other low-energy quadrupole transport lines for Heavy-Ion Fusion. The last row is a more extreme case representing a possible low-energy solenoidal transport lattice under consideration for Heavy-Ion Fusion applications[15]. Final values are tabulated for form-factors $F_a = 1$ (uncorrected), $F_a = |s - s_p|/\sqrt{R^2 + (s-s_p)^2}$ [linear field correction, Eq. (23)], and $F_a(|s - s_p|/R)$ [nonlinear correction, Eq. (16) or Eq. (17)]. Negligible difference is observed between envelope solutions produced with the nonlinear form-factor and the approximate form-factor based on linear plus cubic field terms in Eq. (23). For most applications, deviations between results produced by the linear field approximation and nonlinear form-factors are not significant. The most significant correction for parameters explored is in the envelope angle at the plate $R'(s_p)$ with typical experimentally resolvable[6, 8] errors ~ 1 mrad occurring. Envelope coordinate corrections at the plate in $R(s_p)$ are not resolvable in typical experiments. The values of the final corrected envelope coordinate and angle at the plate depend on the drift length to the plate, the

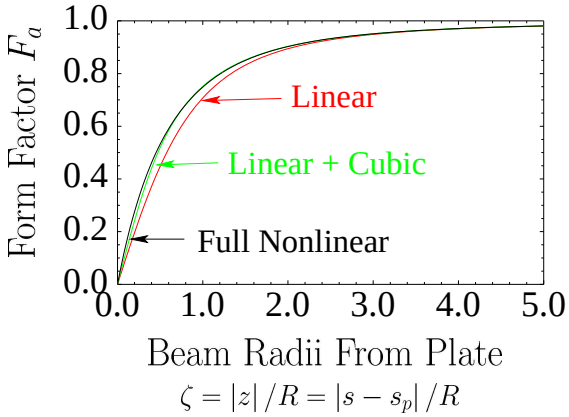

FIG. 5: Form factor F_a for the axisymmetric envelope equation (18) in full nonlinear form [black, Eq. (16) or (17)] and with linear and linear plus cubic nonlinear approximations [red and green, Eq. (23)] plotted versus $\zeta = |s - s_p|/R$.

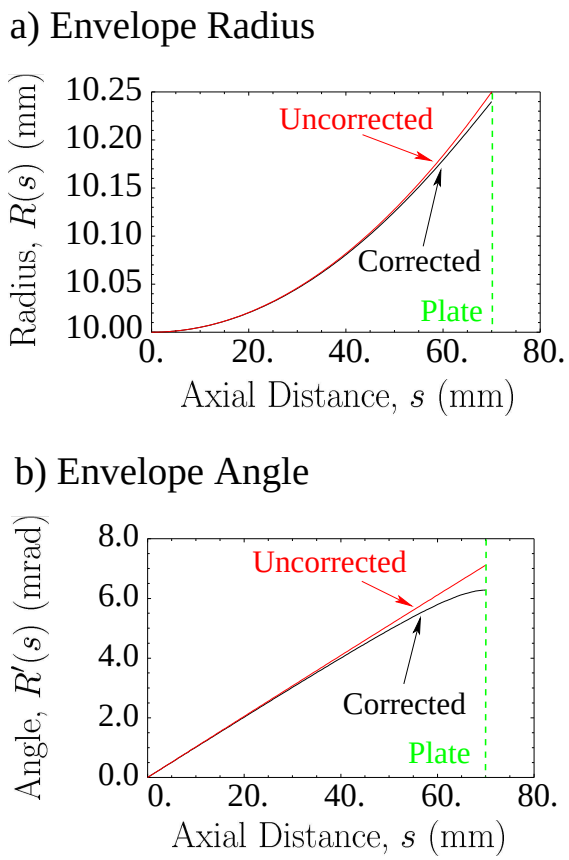

FIG. 6: Evolution of (a) envelope radius R and (b) angle R' given by Eq. (18) for an axisymmetric beam free-drift expanding into a conducting plate. Solutions are given for corrected [black, $F_a(|s - s_p|/R)$] and uncorrected [red, $F_a = 1$] evolutions. Beam parameters are $Q = 10 \times 10^{-4}$ and $\varepsilon = 50$ mm-mrad, the conducting plate is at $s = s_p = 70$ mm, and initial conditions at $s = 0$ are $R(0) = 10$ mm and $R'(0) = 0$.

beam emittance ε, and perveance Q. These dependencies cannot be scaled away. However, we find that deviations between the corrected and uncorrected envelope angles at the plate increases most strongly with increasing values of Q.

Because the envelope angle error induced by the plate is systematic, it can degrade precision beam matching. For example, in the continuous focusing approximation[2], it can be shown that a small-amplitude envelope perturbation $\delta R = R - R_m$ about a matched beam solution with $R = R_m = \text{const}$ with finite initial angle error $\delta R'(0) \neq 0$ and

TABLE I: Initial and final envelope radii and angles for an axisymmetric beam free-drifting from $s = 0$ into a conducting plate at $s = s_p = 70$ mm. Envelope solutions are produced by numerical integration of Eq. (18) with various form-factor models for F_a and self-consistent 3D PIC simulations are produced with the WARP code. Final envelope radii and angles are tabulated for: uncorrected envelope model with $F_a = 1$, linear corrected envelope model F_a [Eq. (23)], full nonlinear envelope model F_a [Eq. (16) or (17)], and PIC simulations.

Beam Parameters		Initial conditions		Final Conditions (R in mm, R' in mrad)							
Perveance, Q	Emittance, ε (mm-mrad)	$R(0)$ (mm)	$R'(0)$ (mrad)	$F_a = 1$ $R(s_p)$	$F_a = 1$ $R'(s_p)$	F_a Linear $R(s_p)$	F_a Linear $R'(s_p)$	F_a Nonlinear $R(s_p)$	F_a Nonlinear $R'(s_p)$	3D PIC $R(s_p)$	3D PIC $R'(s_p)$
$8. \cdot 10^{-4}$	50.	10.	0.	10.20	5.73	10.19	4.99	10.19	5.07	10.18	5.00
$8. \cdot 10^{-4}$	50.	10.	20.	11.59	25.35	11.58	24.63	11.58	24.70	11.57	24.61
$8. \cdot 10^{-4}$	50.	10.	40.	12.98	45.03	12.98	44.32	12.98	44.39	12.96	44.29
$8. \cdot 10^{-4}$	50.	10.	$-20.$	8.81	-13.80	8.80	-14.56	8.80	-14.49	8.79	-14.53
$8. \cdot 10^{-4}$	50.	10.	$-40.$	7.42	-33.21	7.42	-34.00	7.42	-33.92	7.41	-33.94
$8. \cdot 10^{-4}$	100.	10.	0.	10.22	6.24	10.21	5.50	10.21	5.58	10.19	5.53
$8. \cdot 10^{-4}$	50.	15.	0.	15.13	3.77	15.12	3.06	15.12	3.13	15.10	3.06
$5. \cdot 10^{-4}$	50.	10.	0.	10.13	3.66	10.12	3.19	10.12	3.24	10.12	3.19
$10. \cdot 10^{-4}$	50.	10.	0.	10.25	7.11	10.23	6.18	10.24	6.28	10.23	6.20
$15. \cdot 10^{-4}$	50.	10.	0.	10.37	10.54	10.36	9.16	10.36	9.30	10.34	9.19
$100. \cdot 10^{-4}$	125.	25.	0.	25.98	27.71	25.82	19.56	25.84	20.46	25.79	19.71

zero initial coordinate error $\delta R(0) = 0$ will lead to maximum envelope perturbation excursions $\mathrm{Max}[\delta R]$ expressible in two equivalent forms as

$$\begin{aligned} \frac{\mathrm{Max}[\delta R]}{R_m} &= \frac{|\delta R'(0)|}{\sqrt{Q}} \frac{1}{2[1 + 4\sigma_0^2\varepsilon^2/(Q^2 L_p^2)]^{1/4}} \\ &= \frac{|\delta R'(0)|}{\sqrt{Q}} \sqrt{\frac{1 - (\sigma/\sigma_0)^2}{2 + 2(\sigma/\sigma_0)^2}}. \end{aligned} \tag{24}$$

Here, in the first form, σ_0 is the phase advance of oscillations of a single-particle in the applied focusing over one lattice period L_p (in continuous focusing all that matters is the rate of phase accumulation σ_0/L_p, but the expression is written in this form to allow extrapolation to periodic focusing lattices). In the second form, σ/σ_0 is the ratio of single particle phase advances in the presence (σ) and absence (σ_0) of the space-charge of a uniform density matched beam. The space-charge depression σ/σ_0 is a function of $[\sigma_0\varepsilon/(QL_p)]^2$ and satisfies $\lim_{Q\to 0} \sigma/\sigma_0 = 1$. Better estimates for periodic focusing channels can be obtained using results contained in Ref. [2]. However, the simple formulas in Eq. (24) should provide reasonable estimates for periodic focusing channels with $\sigma_0 < 90°$. For the HCX this estimate is consistent with $\delta R' \sim 1$ mrad errors leading to 2–3% mismatch amplitudes. Moreover, systematic errors will occur first at diagnostic stations used to measure mismatch from which re-matchings are calculated and applied to the following lattice and then at subsequent diagnostic stations used to sense the corrected envelope and evaluate the result of the corrections.

Self-consistent WARP PIC simulations were also carried out for beam envelope model solutions presented in Table I and results are also summarized in Table I. General features of the simulations are presented in Sec. III. Simulation parameters in addition to the varied beam parameters listed in the table are given there. The envelope coordinates and angles presented are statistically calculated from the simulated particle distribution with $R = 2^{1/2}\langle x^2 + y^2\rangle_\perp^{1/2}$ and $R' = 2^{1/2}\langle xx' + yy'\rangle_\perp / \langle x^2 + y^2\rangle_\perp^{1/2}$. Potential contours of a simulation are shown in Fig. 7. The contours clearly show the strong influence of the plate on the beam self-field. The simulations agree well with the envelope model results for the small angle corrections and provide strong support for the accuracy of the reduced envelope models derived. Indeed, the level of agreement is surprising for the cases with larger initial envelope angles $R'(0)$ because the envelope model form-factors are derived taking $R = \mathrm{const}$ and therefore do not consistently take into account changes in the envelope radius near the plate. The transverse beam emittances ε_x and ε_y were statistically calculated from the simulated particle distribution using Eq. (7) and typically had $\sim$ 1–2% variations (both increases and decreases) along the axial length of the simulations. These variations were dominated by statistical noise and other numerical errors. The magnitude of of the emittance variations related to nonlinear self-fields of the beam are both too small and too near the plate to induce significant changes in the beam envelope. Little change in simulation results is obtained when the pipe radius of the grounded cylindrical pipe is increased or decreased by factors of two and more. Gridding and particle statistics were checked to make sure that the simulations were well converged. Finally, it is interesting to note from Table I that corrected envelope model results derived with linear self-field form-factor corrections for F_a [Eq. (23)] agree better with the simulations than envelope model results obtained with the form-factor F_a derived

from the full nonlinear self-field model.

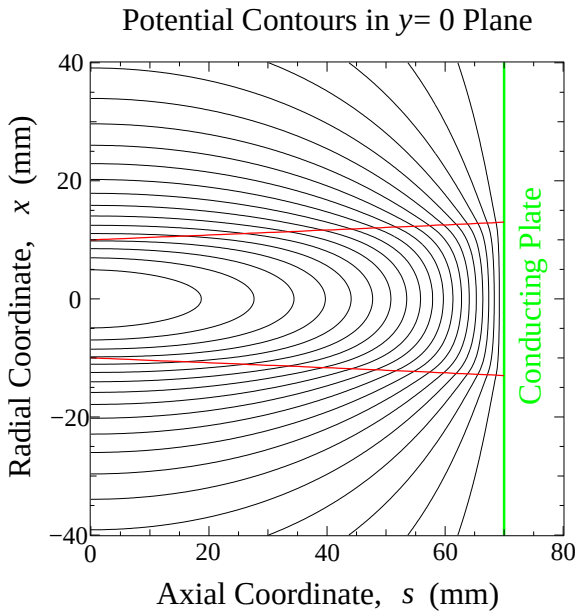

FIG. 7: Self-field potential contours of ϕ and statistical beam envelope R of a WARP PIC simulation of a mid-pulse axisymmetric beam near a conducting plate. Contours are equally spaced in volts in the x–z plane and the statistical envelope projections $x = \pm R$ are shown in red. Beam parameters correspond to those in Table I with $Q = 8 \cdot 10^{-4}$, $\varepsilon = 50$ mm-mrad, $R(0) = 10$ mm, and $R'(0) = 40$ mrad.

V. CORRECTED ENVELOPE EQUATIONS FOR ELLIPTICAL BEAMS

Calculation of the form-factors in Eq. (6) to obtain corrected envelope equations for beams of elliptical cross-section ($r_x \neq r_y$) is considerably more complicated than for the axisymmetric beams analyzed in Sec. IV. However, using the axisymmetric beam results as a guide to motivate model approximations, we present a simple model here that recovers most of the effect of the plates for elliptical beams.

A. Self-Field Solution

To model the beam self-fields, we assume a uniform density, normally incident beam of elliptical cross-section with edge-radii $r_x = \text{const}$ and $r_y = \text{const}$ along the x- and y-axes. In this case the beam density is

$$n(x,y,z) = \frac{\lambda}{\pi q r_x r_y}\Theta\left(1 - \frac{x^2}{r_x^2} - \frac{y^2}{r_y^2}\right)\Theta(-z). \tag{25}$$

The 3D Poisson equation (2) is approximated within the beam (i.e., $x^2/r_x^2 + y^2/r_y^2 \leq 1$ and $z \leq 0$) as

$$\left(\frac{\partial^2}{\partial x^2} + \frac{\partial^2}{\partial y^2}\right)\phi \simeq -\frac{\lambda}{\pi r_x r_y \epsilon_0} + \frac{\partial E_z}{\partial z}(r=0,z) \equiv \frac{\lambda_e}{\pi r_x r_y \epsilon_0}, \tag{26}$$

where we calculate the on-axis electric field $E_z(r=0,z) = -\partial\phi(r=0,z)/\partial z$ exactly from Eqs. (9) and (25) and obtain

$$E_z(r=0,z) = \frac{\lambda}{\pi\epsilon_0}\left(\int_{-\pi}^{\pi}\frac{d\theta}{2\pi}\,\frac{\sqrt{r_x^2\cos^2\theta + r_y^2\sin^2\theta + z^2}}{r_x^2\cos^2\theta + r_y^2\sin^2\theta} - \frac{|z|}{r_x r_y}\right). \tag{27}$$

Equation (27) is derived by differentiating Eq. (9) with respect to z, evaluating the result at $r = 0$, and then taking $\tilde{x} = r_x\tilde{\rho}\cos\tilde{\theta}$, $\tilde{y} = r_y\tilde{\rho}\sin\tilde{\theta}$, and $d^3\tilde{x} = r_x r_y d\tilde{\rho}\tilde{\rho}d\tilde{\theta}d\tilde{z}$ and carrying out integrals with respect to $\tilde{z}$ and $\tilde{\rho}$. As a partial

check of Eq. (27), observe that for a round beam with $r_x = r_y = R$ that this expression reduces to the on-axis field of the axisymmetric beam previously calculated in Eq. (13). Using Eq. (27), we calculate the corrected line-charge density λ_e in Eq. (26) in several equivalent forms as

$$\begin{aligned}\lambda_e &\equiv \lambda - \pi r_x r_y \epsilon_0 \frac{\partial E_z}{\partial z}(r=0,z) \\ &= \frac{2\lambda}{\pi}\frac{r_y\,|z|}{r_x\sqrt{r_x^2+z^2}}\Pi\left(\frac{r_x^2-r_y^2}{r_x^2}\middle|\,\frac{r_x^2-r_y^2}{r_x^2+z^2}\right) \\ &= \frac{2\lambda}{\pi}\frac{r_x\,|z|}{r_y\sqrt{r_y^2+z^2}}\Pi\left(-\frac{r_x^2-r_y^2}{r_y^2}\middle|\,-\frac{r_x^2-r_y^2}{r_y^2+z^2}\right).\end{aligned} \tag{28}$$

Here, $\Pi(a|b)$ is the complete elliptic integral of the third kind defined by $\Pi(a|b) \equiv \int_0^{\pi/2} d\theta\,(1-a\sin^2\theta)^{-1}(1-b\sin^2\theta)^{-1/2}$.

Because the corrected density $\lambda_e/(\pi r_x r_y)$ in Eq. (28) is independent of x and y, the solution to Eq. (26) consistent with a regular external solution at large radius r can be obtained by rescaling the usual transverse 2D field solution of a uniform density elliptical beam[2, 16] with density $\lambda/(\pi r_x r_y)$ by replacing $\lambda \to \lambda_e$ in the usual expressions. This gives within the beam

$$\begin{aligned}-\frac{\partial\phi}{\partial x} &= \frac{\lambda_e}{\pi\epsilon_0}\frac{1}{r_x+r_y}\frac{x}{r_x}, \\ -\frac{\partial\phi}{\partial y} &= \frac{\lambda_e}{\pi\epsilon_0}\frac{1}{r_x+r_y}\frac{y}{r_y}.\end{aligned} \tag{29}$$

B. Corrected Envelope Equations and Results

Using the approximate field solutions in Eq. (29), we calculate the form-factors in Eq. (6) for the elliptical beam as

$$F_x = F_y \equiv F_e = \frac{\lambda_e}{\lambda}. \tag{30}$$

Then using Eq. (28), F_e can be expressed in symmeterized form as

$$F_e(\zeta,\epsilon) = \frac{2}{\pi}\frac{\zeta}{\epsilon\sqrt{\epsilon+\zeta^2}}\Pi\left(1-\frac{1}{\epsilon^2}\middle|\,\frac{\epsilon-1/\epsilon}{\epsilon+\zeta^2}\right). \tag{31}$$

Here, $\epsilon \equiv r_x/r_y$ is the ellipticity of the envelope and $\zeta \equiv |z|/\sqrt{r_x r_y}$ is the axial distance to the plate in average transverse beam radii. These form-factors can be checked in several limits. First, using $\Pi(a|0) = \pi/(2\sqrt{1-a})$, $\lim_{|z|\to\infty} F_e = 1$ follows, and far from the plate the usual form factors for a 2D elliptical beam in free-space are obtained. Next, using $\Pi(0|0) = \pi/2$, in the limit of a round beam with $r_x = r_y = R$, $F_e = |z|/\sqrt{R^2+z^2}$ consistent with the linear-field axisymmetric beam result given in Eq. (23) with $\zeta = |z|/R$. The form-factor $F_e(\zeta,\epsilon)$ is plotted in Fig. 8 versus $\zeta = |z|/\sqrt{r_x r_y} = |s-s_p|/\sqrt{r_x r_y}$ for values of $\epsilon = r_x/r_y$. Because F_e is invariant under the replacement $\epsilon \to 1/\epsilon$, only values of $\epsilon \le 1$ are shown. Qualitatively, the results are similar to the axisymmetric beam results presented in Sec. IV B and there is little variation of F_e in ϵ for all but the most extreme values of ellipticity $\epsilon = r_x/r_y \neq 1$.

To obtain corrected envelope equations for an elliptical beam near a conducting plate, analogously to the axiymmetric case in Sec. IV, in Eq. (4) we heuristically apply the form-factors (31) with $|z| = |s-s_p|$ the distance from the conducting plate and *evolving* beam radii r_x and r_y giving

$$\begin{aligned}r_x'' + \kappa_x r_x - \frac{2Q}{r_x+r_y}F_e\left(\frac{|s-s_p|}{\sqrt{r_x r_y}},\frac{r_x}{r_y}\right) - \frac{\varepsilon_x^2}{r_x^3} = 0, \\ r_y'' + \kappa_y r_y - \frac{2Q}{r_x+r_y}F_e\left(\frac{|s-s_p|}{\sqrt{r_x r_y}},\frac{r_x}{r_y}\right) - \frac{\varepsilon_y^2}{r_y^3} = 0.\end{aligned} \tag{32}$$

Because of the weak dependence of $F_a(\zeta,\epsilon)$ on $\epsilon = r_x/r_y$, in many cases adequate precision can be attained by approximating F_e in Eq. (32) as

$$F_e(\zeta,\epsilon) \simeq F_e(\zeta,1) = \frac{\zeta}{\sqrt{1+\zeta^2}} \tag{33}$$

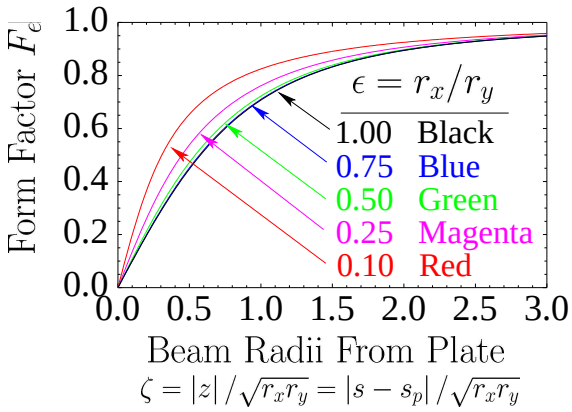

FIG. 8: Form factor F_e [Eq. (31)] for the elliptical beam envelope equations (32) plotted versus $\zeta = |z|/\sqrt{r_x r_y} = |s - s_p|/\sqrt{r_x r_y}$ for values of $\epsilon = r_x/r_y$ indicated.

with $\zeta = |s - s_p|/\sqrt{r_x r_y}$. Note that $F_e(\zeta, 1)$ is the same form factor as for the axisymmetric beam in the linear self-field approximation [see Eq. (23)] with $\zeta = |z|/R$ for the axisymmetric beam replaced by $\zeta = |z|/\sqrt{r_x r_y}$ for the elliptical beam.

Results of the corrected envelope model using Eq. (31) for F_e in numerical integrations of Eq. (32) with $\varepsilon_x = \varepsilon_y =$ const are contrasted to uncorrected envelope model results with $F_e = 1$ and self-consistent 3D WARP PIC simulations in Table II. Geometry and beam parameters are analogous to those presented in Table I. Results are grouped for two separate values of perveance Q showing three initial conditions for each value. The first row in each group is an axisymmetric initial condition directly comparable to cases in Table I for consistency checks. In the simulations, the envelope radii and angles are statistically calculated from the particle distribution as $r_x = 2\langle x^2\rangle_\perp^{1/2}$, $r_y = 2\langle y^2\rangle_\perp^{1/2}$ and $r_x' = 2\langle xx'\rangle_\perp/\langle x^2\rangle_\perp^{1/2}$, $r_y' = 2\langle yy'\rangle_\perp/\langle y^2\rangle_\perp^{1/2}$. Note for this axisymmetric initial condition that the results for the $F_e = 1$ and F_e corrected envelope solutions in Table II are identical to the corresponding results for the $F_a = 1$ and F_a linear envelope solutions in Table I. Moreover, differences in the simulation results between the axisymmetric initial condition results in Table II with the axisymmetric simulation results in Table I as well as differences between r_x and r_y, r_x' and r_y' in the axisymmetric initial condition simulations in Table II are attributable to simulation noise and numerical errors. The good agreement on the final envelope angles between the simulation results and corrected envelope model results in Table II verifies that the linear self-field form-factor corrections in Eq. (31) is adequate for most purposes.

TABLE II: Initial and final envelope radii and angles for axisymmetric and elliptical beam initial conditions free-drifting from $s = 0$ into a conducting plate at $s = s_p = 70$ mm. Final envelope radii are shown for: uncorrected envelope with $F_e = 1$, linear corrected F_e, and 3D self-consistent WARP PIC simulations. Upper and lower table entries have different values of perveance Q.

Beam Parameters: $Q = 10 \cdot 10^{-4}$, $\varepsilon_x = \varepsilon_y = 50$ mm-mrad													
Initial Conditions		Final Conditions (r_x and r_y in mm, r_x' and r_y' in mrad)											
		$F_e = 1$, Uncorrected				F_e Corrected				3D PIC Simulation			
$r_x(0) = r_y(0)$ (mm)	$r_x'(0) = -r_y'(0)$ (mrad)	$r_x(s_p)$	$r_y(s_p)$	$r_x'(s_p)$	$r_y'(s_p)$	$r_x(s_p)$	$r_y(s_p)$	$r_x'(s_p)$	$r_y'(s_p)$	$r_x(s_p)$	$r_y(s_p)$	$r_x'(s_p)$	$r_y'(s_p)$
10.	0.	10.25	10.25	7.11	7.11	10.24	10.24	6.19	6.19	10.24	10.24	6.18	6.20
10.	20.	11.65	8.85	27.08	−12.84	11.64	8.84	26.16	−13.76	11.64	8.84	26.12	−13.72
10.	40.	13.05	7.45	47.06	−32.78	13.04	7.44	46.17	−33.67	13.04	7.44	46.08	−33.61

Beam Parameters: $Q = 15 \cdot 10^{-4}$, $\varepsilon_x = \varepsilon_y = 50$ mm-mrad													
Initial Conditions		Final Conditions (r_x and r_y in mm, r_x' and r_y' in mrad)											
		$F_e = 1$, Uncorrected				F_e Corrected				3D PIC Simulation			
$r_x(0) = r_y(0)$ (mm)	$r_x'(0) = -r_y'(0)$ (mrad)	$r_x(s_p)$	$r_y(s_p)$	$r_x'(s_p)$	$r_y'(s_p)$	$r_x(s_p)$	$r_y(s_p)$	$r_x'(s_p)$	$r_y'(s_p)$	$r_x(s_p)$	$r_y(s_p)$	$r_x'(s_p)$	$r_y'(s_p)$
10.	0.	10.37	10.37	10.54	10.54	10.36	10.36	9.16	9.16	10.34	10.36	9.16	9.19
10.	20.	11.77	8.97	30.51	−9.42	11.75	8.96	29.14	−10.78	11.75	8.96	29.07	−10.72
10.	40.	13.17	7.57	50.49	−29.35	13.15	7.56	49.15	−30.69	13.15	7.55	48.99	−30.59

VI. CONCLUSIONS

Generalized transverse envelope equations were derived to improve modeling of intense ion-beams impinging at normal incidence on a conducting plate. Such intercepting plates are typical in intense beam diagnostics used to measure the transverse phase-space of the particle distribution of the beam. The corrected envelope equations were derived for both beams of axisymmetric and elliptical transverse cross-section by deriving analytical form-factor corrections to the perveance term of the usual envelope equations. Predictions of this envelope model were verified using self-consistent 3D PIC simulations. It was found that form-factors derived under the approximation of simple linear models of the beam self-field had adequate accuracy for most applications. For usual parameters, the main effect of plate is a small, systematic correction in the envelope angle at the plate. This effect is a strong function of the beam perveance. Taking into account this effect enables improved beam matching in intense beam applications.

Acknowledgments

The authors wish to thank P. A. Seidl and L. Prost for motivating the need for this study and providing input on examples derived from the HCX experiment, E. P. Lee for suggesting methods that led to several approximations developed, D. P. Grote and J.-L. Vay for help with the WARP PIC simulations, and J. J. Barnard and A. Friedman for useful discussions.

This research was performed under the auspices of the U.S. Department of Energy by the University of California at the Lawrence Livermore and Lawrence Berkeley National Laboratories under contract Nos. W-7405-Eng-48 and DE-AC03-76SF00098.

[1] M. Reiser, *Theory and Design of Charged Particle Beams* (John Wiley & Sons, Inc., New York, 1994).
[2] S. M. Lund and B. Bukh (2003), *Stability Properties of the Transverse Envelope Equations Describing Intense Ion Beam Transport*, submitted for publication.
[3] F. J. Sacherer, IEEE Trans. Nucl. Sci. **18**, 1105 (1971).
[4] I. Kapchinskij and V. Vladimirskij, in *Proceedings of the International Conference on High Energy Accelerators and Instrumentation* (CERN Scientific Information Service, Geneva, 1959), p. 274.
[5] V. P. Karpenko, P. A. Seidl, R. M. Franks, and S. M. Lund, in *Proceedings of the 2001 Particle Accelerator Conference* (IEEE #01CH37268C. Piscataway, NJ 08855, 2001), p. 1447.
[6] P. A. Seidl, D. Baca, F. M. Bieniosek, A. Faltens, S. M. Lund, A. W. Molvik, L. R. Prost, D. B. Shuman, and W. L. Waldron, Laser and Particle Beams **20**, 435 (2002).
[7] F. Bieniosek, W. B. Ghiorso, and L. Prost, in *Proceedings of the 2003 Particle Accelerator Conference* (Portland, OR, 2003), p. WPPB050.
[8] P. A. Seidl, D. Baca, F. M. Bieniosek, A. Faltens, L. R. Prost, G. Sabbi, W. Waldron, R. Cohen, A. Friedman, S. M. Lund, et al., in *Proceedings of the 2003 Particle Accelerator Conference* (Portland, OR, 2003), p. ROAC001.
[9] D. P. Grote, A. Friedman, I. Haber, W. Fawley, and J.-L. Vay, Nuc. Instr. Meth. A **415**, 428 (1998).
[10] S. M. Lund, J. J. Barnard, and E. P. Lee, in *Proceedings of the XX International Linac Conference* (Monterey, CA, 2001), p. 290 and MOE11.
[11] S. M. Lund and B. Bukh, in *Proceedings of the 2003 Particle Accelerator Conference* (Portland, OR, 2003), p. WPPG022.
[12] J. D. Jackson, *Classical Electrodynamics* (John Wiley & Sons, Inc., New York, 1975), second edition ed.
[13] A. W. Molvik, R. H. Cohen, A. Friedman, S. M. Lund, D. Baca, F. M. Bieniosek, M. A. Furman, E. P. Lee, P. A. Seidl, J.-L. Vay, et al., in *Proceedings of the 2003 Particle Accelerator Conference* (Portland, OR, 2003), p. TOPC004.
[14] R. H. Cohen, S. M. Lund, A. W. Molvik, M. A. Furman, J.-L. Vay, and P. Stoltz, in *Proceedings of the 2003 Particle Accelerator Conference* (Portland, OR, 2003), p. TOAA010.
[15] E. Lee and R. J. Briggs, Tech. Rep. LBNL-40774, UC-419, Lawrence Berkeley National Laboratory (1997).
[16] R. C. Davidson and H. Qin, *Physics of Intense Charged Particle Beams in High Energy Accelerators* (World Scientific, 2001).